



On the Magnetic Protection of the Atmosphere of Proxima Centauri b

K. Garcia-Sage^{1,2}, A. Gloer¹, J. J. Drake³, G. Gronoff^{4,5}, and O. Cohen⁶

¹NASA Goddard Space Flight Center, Greenbelt, MD, USA; katherine.garcia-sage@nasa.gov

²Catholic University of America, Washington, DC, USA

³Harvard Smithsonian Center for Astrophysics, Cambridge, MA, USA

⁴NASA Langley, Hampton, VA, USA

⁵SSAI, Hampton, VA, USA

⁶University of Massachusetts, Lowell, MA, USA

Received 2017 May 6; revised 2017 July 3; accepted 2017 July 8; published 2017 July 24

Abstract

The discovery of exoplanets orbiting red dwarfs, such as Proxima Centauri b, has led to questions of their habitability and capacity to retain liquid surface water. While Proxima b is in a “temperate orbit,” i.e., an Earth at that location would not freeze or boil its oceans, its proximity to a parent star with quite high magnetic activity is likely to influence its atmospheric evolution and habitability. Planetary magnetic fields can prevent direct stripping away of the planetary atmosphere by the stellar wind, but ion escape can still occur at the magnetic poles. This process, the polar wind, is well known to occur at Earth and may have contributed to the habitability of Earth’s early atmosphere. The polar wind is highly variable and sensitive to both ionizing radiation and geomagnetic activity. The higher ionizing radiation levels of M dwarfs at habitable zone distances are expected to increase the polar wind by orders of magnitude and, instead of helping create a habitable atmosphere, may strip away enough volatiles to render the planet inhospitable. Here, we compute the ionospheric outflow of an Earth-twin subject to the enhanced stellar EUV flux of Proxima b, and the effect on atmospheric escape timescales. We show that an Earth-like planet would not survive the escape of its atmosphere at that location, and therefore the pathway to habitability for Proxima b requires a very different atmospheric history than that of Earth.

Key words: planet–star interactions – planetary systems – planets and satellites: atmospheres – planets and satellites: magnetic fields – planets and satellites: terrestrial planets – stars: low-mass

1. Introduction

The discovery of Proxima Centauri b (Anglada-Escudé et al. 2016) and the TRAPPIST-1 system planets (Gillon et al. 2017) in temperate orbits where liquid surface water may be possible presents the potential of habitability for these Earth-mass planets. Proxima Centauri, an M6 dwarf, is cooler and less luminous than the Sun, and its “habitable zone” is much closer to the star. However, the potential for habitability of an M dwarf planet depends also on the atmosphere that the planet is able to maintain (Shields et al. 2016). A number of processes can influence atmospheric content and loss, including Jeans’ escape, hydrodynamic escape, and outgassing from the planetary interior (Tian et al. 2013; Tian 2015 and references therein). Space weather effects present an additional factor that can influence atmospheric content and loss, as well as the radiation environment that can impact habitability (Lammer et al. 2007; Airapetian et al. 2017). In addition to a temperate zone that is relatively close to the star, Proxima Centauri is characterized by high magnetic activity and flaring (e.g., Güdel et al. 2002; Wargelin et al. 2017), resulting in a large and highly variable EUV and X-ray⁷ flux at the closely orbiting habitable zone planet.

Past work detailing exoplanet ion escape (Lammer et al. 2003; Zuluaga et al. 2013), including Proxima b (Ribas et al. 2016), has generally assumed that the presence of a magnetosphere that extends beyond the planet’s exobase is the primary consideration in the protection of the atmosphere from EUV heating and related escape, as well as from the stellar wind that

can strip away the atmosphere. However, a magnetized planet is also subject to atmospheric erosion at the magnetic poles, where open field lines extend from the planet’s surface and into the stellar wind, providing an open pathway for ionospheric escape (e.g., Moore et al. 1999). This pathway, in addition to allowing ion escape, plays a role in regulating energy input from the magnetosphere and stellar wind, resulting in additional acceleration processes beyond purely photochemical ones. Dong et al. (2017) provide a global picture of possible polar escape using a multi-species MHD model with a Venus-like neutral atmospheric composition. In this Letter, we provide a complementary picture of possible polar escape from Proxima b using an Earth-like neutral atmosphere and a 1D model of magnetic field-aligned transport and escape of electrons as well as multiple ion species. Ionospheric plasma processes provide additional energy for atmospheric escape and often act differently on different ion species. As such, they can regulate the composition through allowing escape of ions that may otherwise be gravitationally bound.

Under purely hydrodynamic effects, Earth’s geocorona is composed primarily of hydrogen and some helium. The acceleration of ionized oxygen into the magnetosphere indicates that additional energization processes are effective for ions that enable their escape. These processes include frictional heating between ions and atmospheric neutrals, direct ion heating, for example, from interactions with electromagnetic waves, and electron heating that raises the scale-height of electrons and thereby provides an ambipolar electric field that draws ions up along magnetic field lines (Strangeway et al. 2005; Lotko 2007; Yau et al. 2007 and references therein). The incident EUV spectrum influences several of these processes, both by ionizing the neutral atmosphere to provide the ionospheric source

⁷ Here, we use “X-ray” to refer to the spectral range of 1–100 Å and “EUV” to refer to 100–912 Å.

population and by heating the ionosphere and neutral atmosphere. Current rates of ionospheric outflow at Earth are estimated to be $\sim 72 \times 10^{24} \text{ O}^+ \text{ ions s}^{-1}$ (Seki et al. 2001), but ionospheric escape is believed to have played a role in the pathway to habitability of the atmosphere of early Earth, when the Sun’s flare activity and the resulting ion outflow were much larger (Airapetian et al. 2017).

Here, we present an experiment that places the Earth at the orbit of Proxima b. We use the Polar Wind Outflow Model (Glocer et al. 2009a, 2012) along with an estimate of Proxima Centauri’s ionizing spectrum to predict escape of H^+ and O^+ along open magnetic field lines. We do not know whether Proxima b has a magnetic field, but we assume for the purposes of this experiment that Proxima b’s intrinsic magnetic field strength is identical to that of Earth. A decreased magnetic dipole strength is expected to further enhance the escape, but that is an area for future study. Although we are using the spectrum for Proxima, similar results are likely for the TRAPPIST-1 planets: TRAPPIST-1 appears to have weaker $\text{Ly}\alpha$ emission relative to its bolometric luminosity than Proxima by a factor of ~ 2 but stronger X-ray emission by a factor of ~ 3 (Bourrier et al. 2017; Wheatley et al. 2017).

2. Proxima Centauri EUV and X-Ray Spectrum

Our EUV to X-ray spectrum of Proxima has been tailored to match typical conditions outside of the largest flares but still with a significant level of flaring activity. Since coronal emission from M dwarfs such as Proxima appears to have what amounts to a continuous flaring component (e.g., Kashyap et al. 2002), the choice of which constitutes a typical level of emission is somewhat subjective. A thorough assessment of the historic X-ray activity level of Proxima, beginning with observations with the *Advanced Satellite for Cosmology and Astrophysics* (ASCA) satellite in 1994, has recently been presented by Wargelin et al. (2017). Proxima was also observed by the *Einstein*, *EXOSAT*, and *ROSAT* satellites between 1979 and 1990, although difficulties in understanding the cross-calibration of those observations with data obtained by later missions prevent a precise and unambiguous comparison. Wargelin et al. (2017) described a method to assess the underlying quiescent X-ray emission in *ASCA*, *Swift*, *Chandra*, and *XMM-Newton* observations based on count rate distributions measured in intervals ranging from 100 to 1000 s, depending on source and background count rates. The quiescent rates corresponded to an X-ray luminosity in the 0.5–2.5 keV bandpass of $2\text{--}4 \times 10^{26} \text{ erg s}^{-1}$, and Wargelin et al. (2017) found evidence for a cyclic component to this spread correlated with an optical detection of a magnetic cycle. The cyclic amplitude in quiescent emission amounts to approximately 50%, but this is in general dominated by observation-to-observation scatter in total X-ray luminosity due to flares. To achieve a more typical X-ray irradiance, the quiescent level needs to be combined with some degree of flaring. Moreover, in order to accurately characterize the X-ray spectrum itself, high spectral resolution—such as from *Chandra* or *XMM-Newton* grating observations—is desirable.

Given the situation described above, we based our representative X-ray spectrum on an 80 ks *Chandra* HETG +ACIS-S observation obtained on 2010 December 13. The light curve from the observation exhibits some small flares in which the quiescent rate was seen to increase by factors of a few (see Figure 10 of Wargelin et al. 2017) over periods of

a few ks duration. The HETG spectrum was modeled within the *Sherpa* fitting engine using the APEC optically thin plasma radiative loss model using a six-temperature model in which the temperatures of each component were fixed on a regular logarithmic temperature grid spanning the range $\log T = 6.25\text{--}7.5$ and the emission measure at each temperature was allowed to vary. The overall metal abundances were also allowed to vary in the fit, and our synthetic spectrum adopted the best-fit metallicity of $[\text{M}/\text{H}] = -0.4$ relative to the photospheric abundance mixture of Grevesse & Sauval (1998).

While the *Chandra* HETG spectrum provided the emission measure distribution in the $\log T = 6.25\text{--}7.5$ temperature range, the bulk of the flux in the EUV spectral range originates in cooler plasma. We adopted an emission measure distribution shape in the range $4.0 \leq \log T < 6.25$ based on the study of Sanz-Forcada et al. (2003) that found essentially a universal form to the temperature structure of the transition region and lower corona of active stars. The normalization of this cooler part of the emission measure distribution was adjusted so as to match extreme ultraviolet fluxes measured by the *EUVE* satellite during its all-sky survey (Bowyer et al. 1996) and subsequent spectroscopic observations (Craig et al. 1997), corrected for interstellar medium absorption using a neutral hydrogen column density of $N_{\text{H}} = 4 \times 10^{17} \text{ cm}^{-2}$ (Wood et al. 2001).

The spectrum itself was computed on a 0.1 \AA grid using the *PINTofALE* IDL-based software library (Kashyap & Drake 2002) using emissivities derived from the *CHIANTI* atomic database (Dere et al. 1997; Landi et al. 2013) and the ionization balance of Bryans et al. (2009).

Comparison of our spectrum with the lower-resolution spectral energy distributions (SEDs) of Ribas et al. (2016, 2017), Linsky et al. (2014), and the Measurement of Ultraviolet Spectral Characteristics of Low-mass Exoplanetary Systems (MUSCLES⁸; Youngblood et al. 2016) project reveals very good agreement in the X-ray and shorter-wavelength EUV range (1–400 Å), but significant discrepancies in the 400–900 Å range. Our flux in the 6–100 Å range is 26% and 2% lower than those of Ribas et al. (2016) and Ribas et al. (2017), respectively. In the 100–400 Å range, our fluxes are 10% lower than those of both Ribas et al. works, about 15% higher than those of Linsky et al. (2014), and within 15% of MUSCLES. Given the considerable variability of Proxima in the EUV to X-ray range, these fluxes are all essentially identical. In the case of the 100–400 Å range this is not surprising, as all are largely based on the same *EUVE* observations, while MUSCLES employs the Linsky et al. (2014) scaling.

In the 400–912 Å range, our flux is instead about 70% higher than the Linsky et al. (2014) based flux of Ribas et al. (2017, which the authors revised upward by a factor of 2.5 from their 2016 assessment), but a factor of 5 larger than that of Linsky et al. (2014) that employed $\text{Ly}\alpha$ scaling and about a factor of 20 larger than that of MUSCLES that derives from the same approach. The discrepancy can mostly be attributed to a large dip in flux in the MUSCLES SED at 400 Å that extends to the Lyman edge. This flux level lies beneath that predicted by the hot $\log T(K) \geq 6.4$ plasma in our model alone. These discrepancies serve as a reminder of the

⁸ <http://cos.colorado.edu/~kevinf/muscles.html>

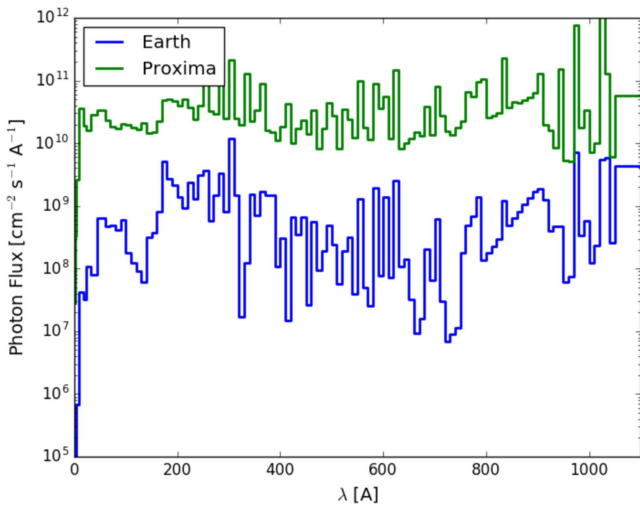


Figure 1. Incident stellar flux ($\text{ph cm}^{-2} \text{s}^{-1} \text{\AA}^{-1}$) at Proxima Centauri b (green) as compared to Earth (blue).

uncertainties in our current knowledge of the EUV fluxes of planet-hosting stars.

Figure 1 shows our resulting spectrum at the orbit of Proxima Centauri b. We also show the spectrum of incident radiation at Earth. In the EUV range, the flux at Proxima b is about two orders of magnitude higher than that at Earth. These spectra are used as input into the outflow model, and the results are discussed below.

3. EUV-enhanced Ionospheric Escape

The Polar Wind Outflow Model (PWOM) has been developed and used extensively to model ionospheric escape at Earth and other magnetized planets (Glocer et al. 2007, 2009a, 2009b, 2012). The model solves the magnetic field-aligned gyrotropic transport equations for multiple ions—in this case H^+ , O^+ , and He^+ —and electrons from a 200 to 8000 km altitude. Neutral densities and temperatures are required as input to the model in order to determine ionization rates and collisional heating of the ionosphere. A chemical equilibrium solution is used for the ion and electron densities at the lower boundary. At the altitudes of interest here, N^+ production is low and may be neglected.

The specification of neutrals presents a major source of uncertainty. We expect that enhanced EUV, as well as enhanced driving from stellar wind interactions with the planetary magnetic field, will increase neutral thermospheric temperatures (Smithro & Sojka 2005). In the context of an Earth-like upper atmosphere subject to intense stellar flaring, it is likely that NO production would help cool down the atmosphere and prevent hydrodynamic escape (Tian et al. 2008; Knipp et al. 2017). The neutral temperature is not modeled self-consistently with the EUV spectrum and magnetospheric-driven heating, but instead a range of neutral temperatures are used in order to demonstrate the dependence of escape on atmospheric heating and cooling. The modeled thermospheric temperatures are based on the MSIS-90 (mass spectrometer and incoherent scatter) empirical model (Hedin 1991) for neutral densities and temperatures in Earth’s thermosphere. We carry out one simulation using the EUV spectrum from Proxima and the thermospheric density and temperature from MSIS-90 for moderately active conditions and

three additional simulations multiplying MSIS-90 temperatures by factors of 2, 3, and 4, in order to explore the possible range of escape rates.

Superthermal electrons from photo- and secondary electron production are calculated using the GLOW model (Solomon et al. 1988; Solomon & Abreu 1989), a two-stream electron transport model that describes the superthermal electron population. This population enhances the heating and ambipolar electric field that enhances upward ion acceleration along magnetic field lines. Thermal electron and ion transport along the magnetic field are simulated in the PWOM model with ambipolar field and electron heating effects, as well as ionization rates from the coupled GLOW model. Details of the superthermal electron coupling can be found in Glocer et al. (2012). Superthermal electron effects, as well as ion production and heating, enable escape of ionospheric ions, particularly heavier species like O^+ that may not be able to escape through purely hydrodynamic processes.

The simulations we carry out here are run until a steady state is achieved, so they do not take into account time-dependent effects. They also do not include effects of wave–particle interactions or electrons precipitating from the magnetosphere, both of which occur in Earth’s ionosphere and enhance ionospheric outflow. The simulations described below, therefore, can be understood as a lower limit on ionospheric escape from Proxima b.

4. Simulation Results

We show five simulations as described above—one Earth case and four Proxima b cases at different thermospheric temperatures. The higher EUV flux at Proxima b increases the photoelectron and secondary production in the two-stream model. The resulting omnidirectional flux of superthermal electrons at altitudes within the coupled two-stream-outflow model is shown in Figure 2, for the Earth spectrum in the top panel and the Proxima b spectrum in the bottom panel. The energy-integrated quantities of total ionization rate, electron heating rate, and superthermal electron flux as a function of altitude are shown in Figure 3. The ionization rate for Proxima b is significantly higher than for Earth due to both the higher EUV flux and electron fluxes that lead to increased secondary production. The heating rate likewise increases due to both the increase in superthermal fluxes and the increase in the thermal electron density. The superthermal electron flux is about an order of magnitude larger at Proxima b, as compared to Earth. The four different thermospheric temperature simulations are shown in these plots, but for the superthermal electrons in the two-stream model, the ionization rate, heating rate, and electron flux depend primarily on the stellar EUV fluxes.

The number density for H^+ , O^+ , and thermal electrons, shown in Figure 4, all increase by at least an order of magnitude relative to the Earth case at the top of the PWOM domain, due to the increased scale heights for the Proxima b case. The outgoing fluxes of these three species also increase. H^+ flux increases by about an order of magnitude, but the largest change is in the O^+ flux. At Earth, there is little to no escape of O^+ without some additional energy input in the form of electromagnetic waves or particle precipitation from the magnetosphere. At Proxima b, the EUV flux alone results in outgoing fluxes of $5.6 \times 10^8 \text{ cm}^{-2} \text{ s}^{-1}$ at 1600 km, while increasing the

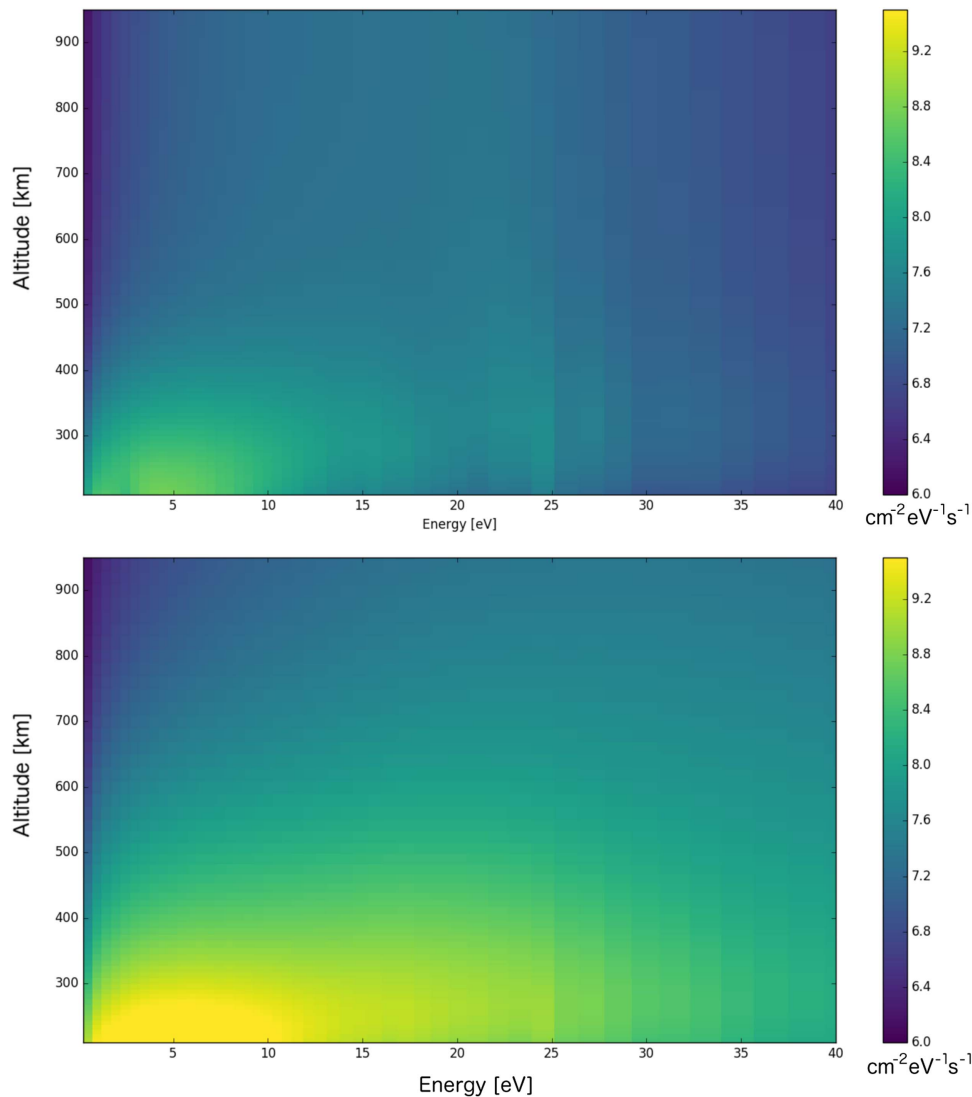


Figure 2. Omnidirectional flux of photoelectrons and secondary electrons, based on incident EUV fluxes at Earth (top) and Proxima Centauri b with thermospheric temperatures of $4 \times T$ (bottom) where T is the temperature of the Earth under moderately active conditions.

thermospheric temperature results in fluxes of 1.8×10^9 ($2 \times T$), 4.2×10^9 ($3 \times T$), and 2.1×10^{10} ($4 \times T$).

5. Discussion and Conclusion

An interesting, albeit less extreme, analog to the current problem is the effect of seasonal and solar cycle variations on ion outflow at Earth. In that problem, like the present simulations, the outflowing O^+ flux shows much larger sensitivity to the solar EUV than does H^+ . The modeled effects of an enhanced EUV spectrum on outflowing ion flux are consistent with observations at Earth that show O^+ remains gravitationally bound in cases of low energy input but is strongly affected by additional EUV flux in the summer hemisphere and at solar maximum (Yau & Andre 1997; Peterson et al. 2008). The simulations shown in this Letter are consistent with that picture of the sensitivity of O^+ to enhanced EUV radiation. Studies at Earth have also indicated that O^+ fluxes are enhanced by charged particle precipitation (Zeng & Horwitz 2007), magnetic field-aligned currents (McFadden et al. 1998), and wave-particle interactions (Crew et al. 1990). These processes are not accounted for in the simulations shown

here. If any of these are present due to magnetospheric dynamics at Proxima b, they may further enhance atmospheric escape.

An additional source of uncertainty is the appropriate long-term average X-ray and EUV flux. We have estimated a “typical” representative spectrum, but very large flares and possible contributions to ionization from energetic protons have not been considered. Both electromagnetic flux and energetic particle flux associated with flares can increase the lower-altitude ionization and heating rates and thereby indirectly enhance ion escape. Proper treatment of flares will require time-dependent calculations that we defer to future work.

Stellar wind effects present additional sources of uncertainty, through frictional heating between ions and neutrals, as well as through influencing the area over which ion flux can escape. The size of the polar cap region that is magnetically connected to the star is affected by the stellar magnetic field strength and direction compared to the planetary magnetic field orientation (Garraffo et al. 2016). In the case of a stronger stellar wind or weaker planetary magnetic field, the region over which the escape can happen may also increase.

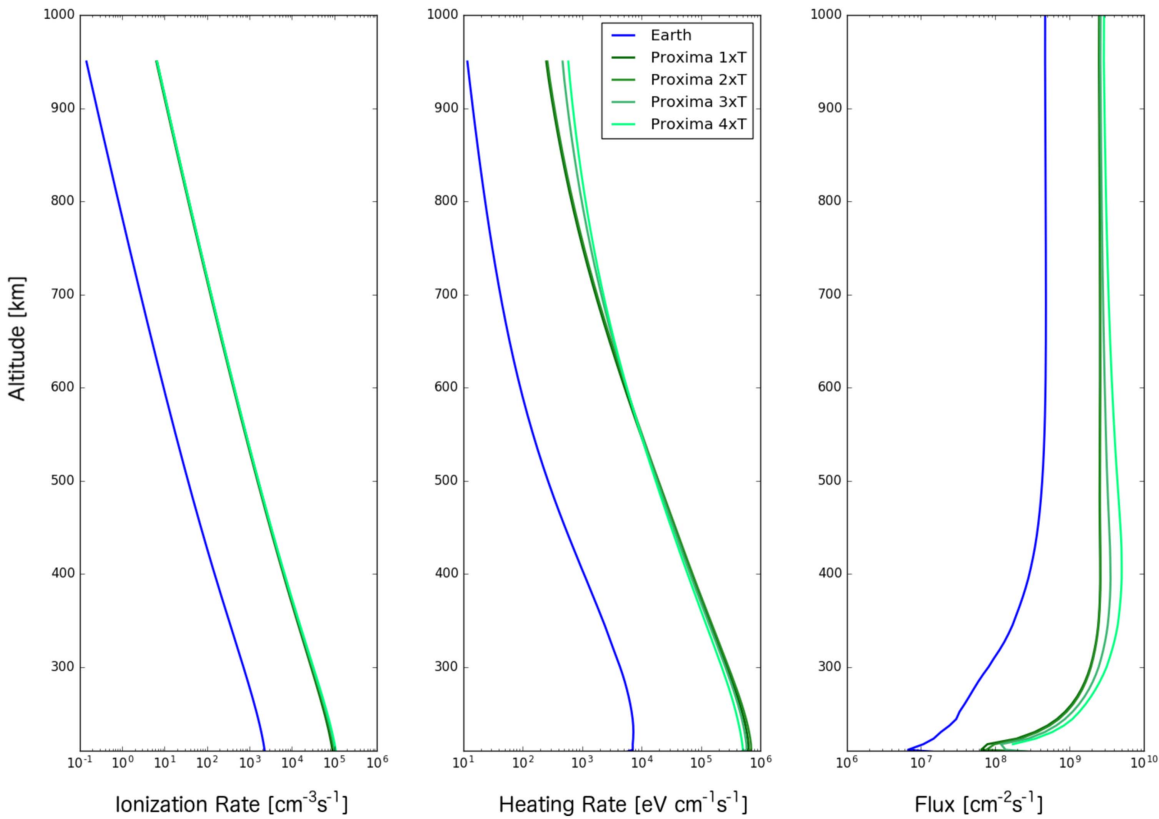


Figure 3. Ionization rate, electron heating rate, and superthermal electron flux in the overlap region of PWOM and two-stream models, for Earth, and for four different thermospheric temperatures at Proxima b.

Rather than self-consistently modeling the effects discussed above, we show the modeled ion outflow for a range of heating and polar cap size. These are the two major pathways through which EUV, energetic particle, and stellar wind effects will influence outflow. A factor of four increase in thermospheric temperature increases the outflowing O^+ fluxes by more than an order of magnitude. The lower open magnetic fluxes (higher latitudes) correspond to the Earth case under quiet to moderate conditions, with an open region down to 60° invariant latitude. At an altitude of 1600 km, 26.6° invariant latitude corresponds to all magnetic fluxes being open, resulting in escape over the entire dayside hemisphere.

These simulations differ from those of Dong et al. (2017) in the presence and self-consistent treatment of the ambipolar E-field, as well as the differential treatment of ions by species. Here, we show a more complete picture of ion and electron transport. However, the Dong et al. (2017) results include a more self-consistent calculation of open magnetic flux, and their findings, along with recent work on stellar wind effects in the similar TRAPPIST-1 system (Garraffo et al. 2017), strongly indicate that the loss rates should be at the open flux end of Figure 5, due to the extremely large polar cap area. The electron effects modeled here enhance ion escape and so our final escape rates of O^+ are larger than the Dong et al. (2017) results for a magnetized planet and are on par with their results for an unmagnetized planet.

With an O^+ and H^+ escape at 1600 km altitude of $4.2 \times 10^9 \text{ cm}^{-2} \text{ s}^{-1}$ as found for thermospheric densities of $3 \times T$, the total mass-loss rate is $4.3 \times 10^5 \text{ g s}^{-1}$ over the dayside hemisphere. Using a total atmospheric mass of $5 \times 10^{18} \text{ kg}$

(Trenberth & Smith 2005) results in a loss of the entire mass of the atmosphere over 365 million years.

The mass loss calculated here is slightly less than that estimated by Airapetian et al. (2017). The difference with Airapetian et al. (2017) can be attributed to different assumptions for the total atmospheric content and nightside escape (which we assume here to be much less than the dayside escape rate), as well as the use of the Proxima Centauri spectrum. We have also carried out full simulations of the effect of the thermospheric temperature on escape, rather than relying on outflow scaling with thermospheric temperature as done in Airapetian et al. (2017).

We emphasize that the timescales presented here are a conservative estimate within large uncertainties. Moreover, Proxima is currently lying somewhat below magnetic activity saturation (Wright & Drake 2016) and would have had higher EUV and X-ray emission levels by up to an order of magnitude in the past. The current results indicate that caution should be used when discussing the potential habitability of Proxima b. The presence of a magnetosphere is not enough to prevent significant atmospheric loss through ionospheric heating and escape. These results do not guarantee that Proxima b is not habitable; a path to habitability would be the replenishment of its atmosphere through outgassing or precipitation of volatiles. From Holland (2002), the present-day net repopulation rate from H_2^+ and O_2^+ is $3 \times 10^6 \text{ g s}^{-1}$. Compared to the loss rates of 5×10^3 to $2 \times 10^6 \text{ g s}^{-1}$ calculated here, repopulation through geologic processes is possible, but the exact balance of processes that influence atmospheric content will be different than at Earth. The escape rates calculated here for H^+ and O^+ may also be larger than escape rates for heavier ion species and

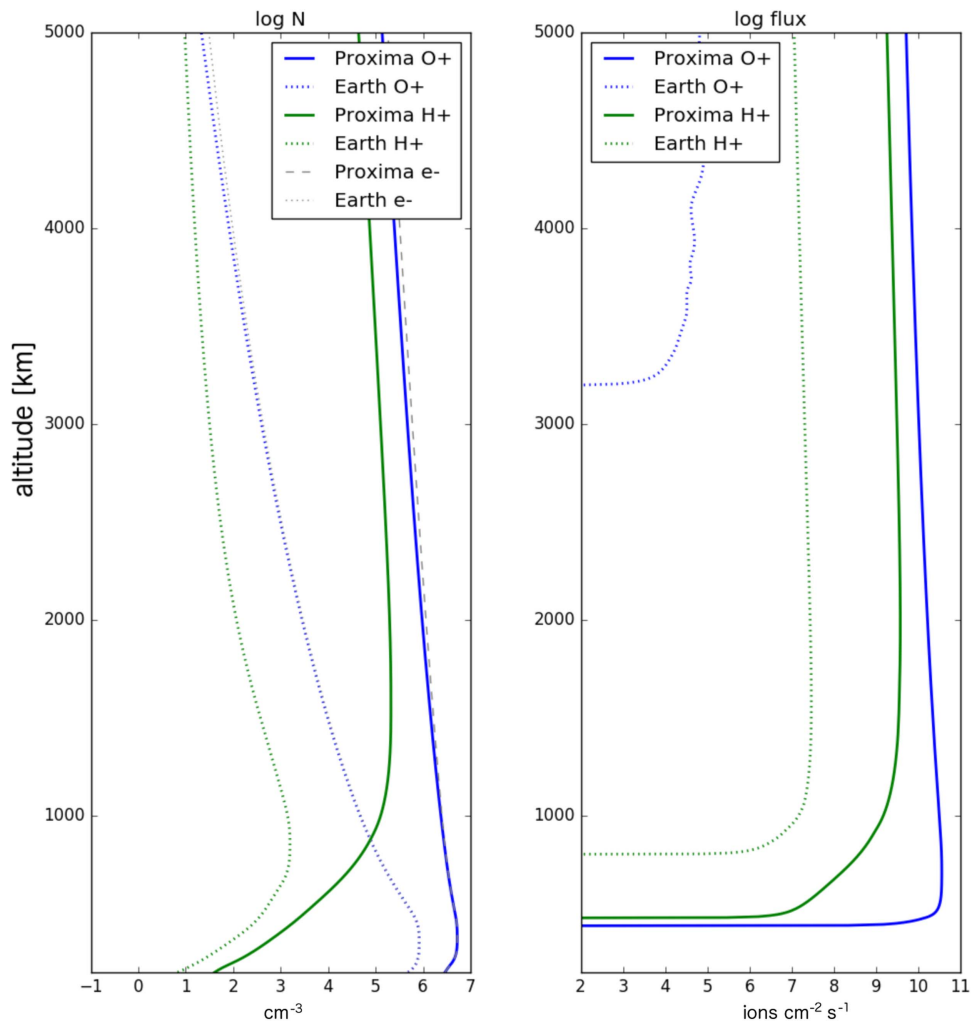


Figure 4. Number density of electrons and ions (left) and outgoing flux of ions (right) in the PWOM model. Dotted lines indicate densities and fluxes at Earth. O^+ flux is absent in this case because without additional energy input, O^+ remains gravitationally bound under moderate solar EUV fluxes. Solid and dashed lines indicate densities and fluxes under stellar flux conditions at Proxima b with a temperature of $4 \times T$. All scale heights increase, and O^+ and H^+ fluxes are of the same order of magnitude at Proxima b.

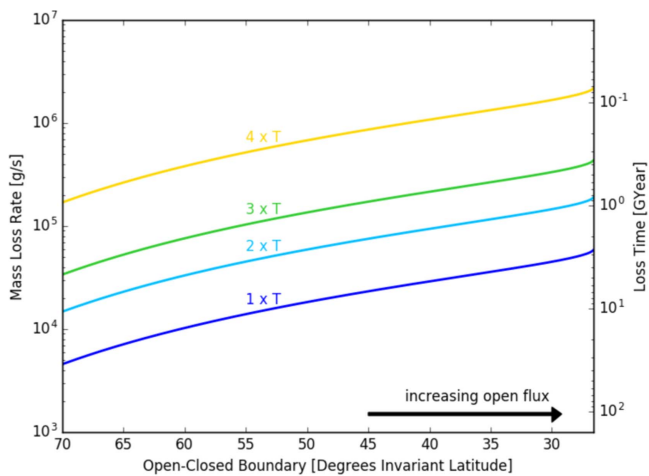


Figure 5. Loss rates and loss timescales at Proxima b as a function of the thermospheric temperature and open magnetic flux. The four curves correspond, in order from top to bottom, to $4 \times T$, $3 \times T$, $2 \times T$, and $1 \times T$, where T is the thermospheric temperature of Earth during moderately active times. The lower limit of the open closed boundary, corresponding to about 26.6° invariant latitude, is the point at which all magnetic flux is open at 1600 km altitude.

molecules, which will influence the overall composition of the planet. However, the large escape rates compared to Earth indicate that, even in the case of an Earth-like intrinsic magnetic field, the evolution of the atmosphere of Proxima b would be very different from that of the Earth.

We thank Stan Solomon for making the GLOW model available for use with PWOM. K.G.-S. and A.G. are supported by the NASA Astrobiology NExSS program. O.C. and G.G. are supported by NASA Astrobiology Institute grant NNX15AE05G. G.G. is supported by the NASA HIDE Program.

References

Airapetian, V. S., Glozer, A., Khazanov, G. V., et al. 2017, *ApJL*, 836, L3
 Anglada-Escudé, G., Amado, P. J., Barnes, J., et al. 2016, *Natur*, 536, 437
 Bourrier, V., Ehrenreich, D., Wheatley, P. J., et al. 2017, *A&A*, 599, L3
 Bowyer, S., Lampton, M., Lewis, J., et al. 1996, *ApJS*, 102, 129
 Bryans, P., Landi, E., & Savin, D. W. 2009, *ApJ*, 691, 1540
 Craig, N., Abbott, M., Finley, D., et al. 1997, *ApJS*, 113, 131
 Crew, G. B., Chang, T., Retterer, J. M., Peterson, W. K., & Gurnett, D. A. 1990, *JGR*, 95, 3959

- Dere, K. P., Landi, E., Mason, H. E., Monsignori Fossi, B. C., & Young, P. R. 1997, *A&AS*, **125**, 149
- Dong, C., Lingam, M., Ma, Y., & Cohen, O. 2017, *ApJL*, **837**, L26
- Garraffo, C., Drake, J. J., & Cohen, O. 2016, *ApJL*, **833**, L4
- Garraffo, C., Drake, J. J., Cohen, O., Alvarado-Gómez, J. D., & Moschou, S. P. 2017, *ApJL*, **843**, L33
- Gillon, M., Triaud, A. H. M. J., Demory, B.-O., et al. 2017, *Natur*, **542**, 456
- Glocer, A., Gombosi, T. I., Toth, G., et al. 2007, *JGRA*, **112**, A01304
- Glocer, A., Kitamura, N., Toth, G., & Gombosi, T. 2012, *JGRA*, **117**, 4318
- Glocer, A., Tóth, G., Gombosi, T., & Welling, D. 2009a, *JGRA*, **114**, A05216
- Glocer, A., Tóth, G., Ma, Y., et al. 2009b, *JGRA*, **114**, A12203
- Grevesse, N., & Sauval, A. J. 1998, *SSRv*, **85**, 161
- Güdel, M., Audard, M., Skinner, S. L., & Horvath, M. I. 2002, *ApJL*, **580**, L73
- Hedin, A. E. 1991, *JGR*, **96**, 1159
- Holland, H. D. 2002, *GeCoA*, **66**, 3811
- Kashyap, V., & Drake, J. J. 2002, in ASP Conf. Ser. 277, Stellar Coronae in the Chandra and XMM-NEWTON Era, ed. F. Favata & J. J. Drake (San Francisco, CA: ASP), 509
- Kashyap, V. L., Drake, J. J., Güdel, M., & Audard, M. 2002, *ApJ*, **580**, 1118
- Knipp, D., Pette, D., Kilcommons, L., et al. 2017, *SpWea*, **15**, 325
- Lammer, H., Lichtenegger, H. I. M., Kulikov, Y. N., et al. 2007, *AsBio*, **7**, 185
- Lammer, H., Selsis, F., Ribas, I., et al. 2003, *ApJL*, **598**, L121
- Landi, E., Young, P. R., Dere, K. P., Del Zanna, G., & Mason, H. E. 2013, *ApJ*, **763**, 86
- Linsky, J. L., Fontenla, J., & France, K. 2014, *ApJ*, **780**, 61
- Lotko, W. 2007, *JASTP*, **69**, 191
- McFadden, J. P., Carlson, C. W., Ergun, R. E., et al. 1998, *GeoRL*, **25**, 2021
- Moore, T. E., Lundin, R., Alcayde, D., et al. 1999, *SSRv*, **88**, 7
- Peterson, W. K., Andersson, L., Callahan, B. C., et al. 2008, *JGRA*, **113**, A07222
- Ribas, I., Bolmont, E., Selsis, F., et al. 2016, *A&A*, **596**, A111
- Ribas, I., Gregg, M. D., Boyajian, T. S., & Bolmont, E. 2017, *A&A*, **603**, A58
- Sanz-Forcada, J., Brickhouse, N. S., & Dupree, A. K. 2003, *ApJS*, **145**, 147
- Seki, K., Elphic, R. C., Hirahara, M., Terasawa, T., & Mukai, T. 2001, *Sci*, **291**, 1939
- Shields, A. L., Ballard, S., & Johnson, J. A. 2016, arXiv:1610.05765
- Smithro, C. G., & Sojka, J. J. 2005, *JGRA*, **110**, A08306
- Solomon, S. C., & Abreu, V. J. 1989, *JGR*, **94**, 6817
- Solomon, S. C., Hays, P. B., & Abreu, V. J. 1988, *JGR*, **93**, 9867
- Strangeway, R. J., Ergun, R. E., Su, Y.-J., Carlson, C. W., & Elphic, R. C. 2005, *JGRA*, **110**, A03221
- Tian, F. 2015, *AREPS*, **43**, 459
- Tian, F., Chassefière, E., Leblanc, F., & Brain, D. 2013, in Comparative Climatology of Terrestrial Planets, ed. S. J. Mackwell et al. (Tucson, AZ: Univ. Arizona Press), 567
- Tian, F., Kasting, J. F., Liu, H. L., & Roble, R. G. 2008, *JGRE*, **113**, 1
- Trenberth, K. E., & Smith, L. 2005, *JCLI*, **18**, 864
- Wargelin, B. J., Saar, S. H., Pojmański, G., Drake, J. J., & Kashyap, V. L. 2017, *MNRAS*, **464**, 3281
- Wheatley, P. J., Louden, T., Bourrier, V., Ehrenreich, D., & Gillon, M. 2017, *MNRAS*, **465**, L74
- Wood, B. E., Linsky, J. L., Müller, H.-R., & Zank, G. P. 2001, *ApJL*, **547**, L49
- Wright, N. J., & Drake, J. J. 2016, *Natur*, **535**, 526
- Yau, A. W., Abe, T., & Peterson, W. K. 2007, *JASTP*, **69**, 1936
- Yau, A. W., & Andre, M. 1997, *SSRv*, **80**, 1
- Youngblood, A., France, K., Parke Loyd, R. O., et al. 2016, *ApJ*, **824**, 101
- Zeng, W., & Horwitz, J. L. 2007, *GeoRL*, **340**, 6103
- Zuluaga, J. I., Bustamante, S., Cuartas, P. A., & Hoyos, J. H. 2013, *ApJ*, **770**, 23